PHYSICAL REVIEW C VOLUME 51, NUMBER 1 JANUARY 1995

Pion inelastic scattering to low-lying positive-parity states in ^{20}Ne

M. Burlein,* H. T. Fortune, W. M. Amos, T. L. Ekenberg, A. Kotwal,† P. H. Kutt, J. M. O'Donnell,‡ and J. D. Silk*
University of Pennsylvania, Philadelphia, Pennsylvania 19104

B. Boyer, A. Fuentes, K. Johnson, C. F. Moore, and S. H. Yoo
University of Texas at Austin, Austin, Texas 78712

S. Mordechai
University of Texas at Austin, Austin, Texas 78712
and Ben-Gurion University of the Negev, Beer-Sheva 84105, Israel

C. L. Morris
Los Alamos National Laboratory, Los Alamos, New Mexico 87545

J. D. Zumbro§
University of Pennsylvania, Philadelphia, Pennsylvania 19104
and Los Alamos National Laboratory, Los Alamos, New Mexico 87545

D. L. Watson
University of York, York Y01-5DD, United Kingdom
and Los Alamos National Laboratory, Los Alamos, New Mexico 87545

K. S. Dhuga‖
New Mexico State University, Los Cruces, New Mexico 88003
(Received 30 March 1994)

We have measured pion inelastic scattering from ^{20}Ne with 180 MeV π^+ and π^- at 12° and from 15° to 90° in 5° steps and with 120 MeV π^+ from 15° to 90° in 5° steps. We report here on states in the first four $K^\pi = 0^+$ bands, including the 6.73-MeV 0^+ and the 8.78-MeV 6^+ levels. Coupled-channels processes are shown to be important for many states.

PACS number(s): 25.80.Ek, 27.30.+t, 21.60.Cs, 21.60.Ev

I. INTRODUCTION

We have measured pion inelastic scattering from ^{20}Ne looking for the effects of two-step reaction routes. Because of its strong rotational structure and because the strengths of many of its transitions have already been measured [1], ^{20}Ne is an ideal nucleus in which to search for two-step routes. Several states have a very weak decay to the ground state, but have a strong branch to the 1.63-MeV 2_1^+. The known ground-state strengths of states in the $K^\pi = 0^+$ bands are shown in the fourth column of Table I. Inelastic scattering from ^{20}Ne has been measured with many other probes, including electrons [2], protons [4], and α's [5]. From these measurements, ^{20}Ne is known to have a strong quadrupole and hexadecapole deformation, $\beta_2 = +0.47 \pm 0.04$ and $\beta_4 = +0.28 \pm 0.05$.

II. EXPERIMENT

We measured pion inelastic scattering from ^{20}Ne using both π^+ and π^- at 180 MeV at 12° and from 15° to 90° in 5° steps. We also acquired data at 120 MeV using only π^+ from 15° to 90° in 5° steps. The data were measured at the Energetic Pion Channel and Spectrometer (EPICS) of the Clinton P. Anderson Meson Physics Facility (LAMPF). The target material was ^{20}Ne gas enriched to > 99.9% purity. The target was kept in a cylindrical steel gas cell at 138 kPa and cooled to 45 K giving an effective areal density of $\sim$100 mg/cm^2 in the middle of the gas cell. Measurements were made at several angles with both π^+ and π^- with an empty target to determine the contribution of the gas cell to the spectra. The resolu-

---

*Present address: Institute for Defense Analysis, 1801 N. Beauregard Street, Alexandria, VA 22311.

†Present address: Fermilab, P.O. Box 500, Batavia, IL 60510.

‡Present address: University of Minnesota, School of Physics, Minneapolis, MN 55455.

§Present address: Los Alamos Meson Physics Facility, Los Alamos National Laboratory, Los Alamos, NM 87545.

‖Present address: George Washington University, Washington, DC 20052.

TABLE I. Ground-state transition strengths in ^{20}Ne.

E_x^a (MeV)	$J^{\pi a}$	$K^{\pi a}$	$B(E\lambda)$ ($e^2\,\mathrm{fm}^{2\lambda}$) (Comp.)[a]	$B(E\lambda)$ ($e^2\,\mathrm{fm}^{2\lambda}$) (ZBM calc.)	$B(E\lambda)$ ($e^2\,\mathrm{fm}^{2\lambda}$) [$(sd)^4$ calc.]	$B(E\lambda)$ ($e^2\,\mathrm{fm}^{2\lambda}$) (measured)[b]
1.63	2^+	0_1^+	335±21	233	303	322.9±1.8
4.24	4^+	0_1^+	3 800±8 000[c]	2 873	27 600	42 400±600
8.78	6^+	0_1^+	-	-	-	$2.2\pm0.9 \times 10^6$
7.42	2^+	0_2^+	0.82±0.17	0.255	0.163	2.9±0.4
9.99	4^+	0_2^+	5.6×10^6	3537	1 160	5 000±600
7.83	2^+	0_3^+	12.0±0.5	4.52	-	16.6 ±0.5
9.03	4^+	0_3^+	-	461	-	9 800±900
9.00	2^+	0_4^+	-	-	-	40.9±2.0
10.79	4^+	0_4^+	-	-	-	6 000±300

[a] Reference [1].

[b] All $B(E\lambda)$'s were obtained by fitting 180-MeV π^+ and π^- data simultaneously with the constraint $M = M_n = M_p$ where $B(E\lambda) = |M_p|^2$. The errors given are statistical only.

[c] Reference [3].

tion was 180-keV full width at half maximum. Absolute normalizations, as a function of angle, were obtained by filling the gas cell with H_2 gas, measuring π-p scattering, and comparing the yields with cross sections calculated from the π-nucleon phase shifts of Rowe, Salomon, and Landau [6]. Relative normalizations are believed to be known to within 4% and absolute normalizations to within 10%.

A ^{20}Ne$(\pi^+,\pi'^+)^{20}$Ne spectrum measured at 30° with T_π=180 MeV is displayed in Figs. 1 and 2. The spectra are dominated by the elastic-scattering peak and the 1.63-MeV 2_1^+ as seen in Fig. 1. The 5.62-MeV 3_1^-, 7.16-MeV 3_2^-, and 4.25-MeV 4_1^+ are also very strong as shown in Fig. 2. A spectrum of states in the region 7–10.5 MeV has already been published [7]. The spectra were fitted using a linear background (dashed line) and constraining the peak energies at their known values for states in ^{20}Ne. The peak shape for the narrow states was determined by fitting the elastic peak shape. The areas of the peaks were the only parameters allowed to vary. The peak shape for states with large natural widths were constrained to be Lorentzians of width Γ, where Γ is the natural width of the state, convoluted with the empirical elastic peak shape. All of the 2^+'s and 4^+'s in the first four $K^\pi = 0^+$ bands are present in the spectra. The 6.73-MeV 0^+ and the 8.78-MeV 6^+ are also seen. Several higher 0^+ bands have been identified in ^{20}Ne but there is no evidence for states from those bands in the data. Angular distributions for these states are displayed in Figs. 3–8.

III. ANALYSIS

Shell-model calculations of the structure of the low-lying states in ^{20}Ne were performed using OXBASH [8] to provide microscopic transition densities. Two sets of calculations were done. The first assumed an ^{16}O closed core and four particles in the *sd* shell, referred to here as $(sd)^4$. This calculation used the *usd* interaction of Wildenthal [9]. The first two rotational bands of ^{20}Ne are believed to be primarily $(sd)^4$ configurations [10] and should be described by this calculation. The second calculation assumed a ^{12}C closed core and eight particles in the $p_{1/2}, d_{5/2}$, and $s_{1/2}$ orbitals, referred to here as ZBM. This model space was first used by Zuker, Buck, and Mc-

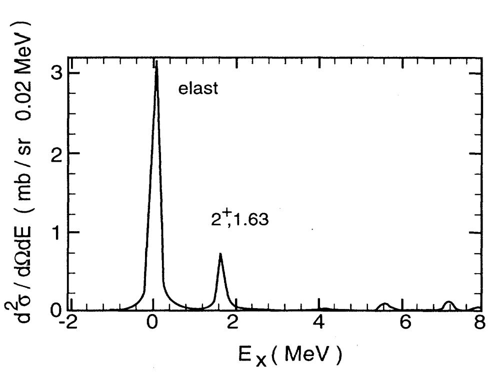

FIG. 1. Fitted missing mass spectrum for ^{20}Ne(π^+,π'^+) at 30° with T_π=180 MeV from −2 to 8 MeV excitation.

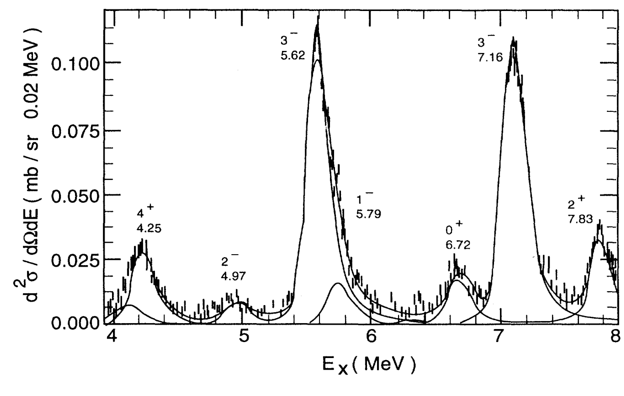

FIG. 2. Same as Fig. 1 but for 4–8 MeV excitation.

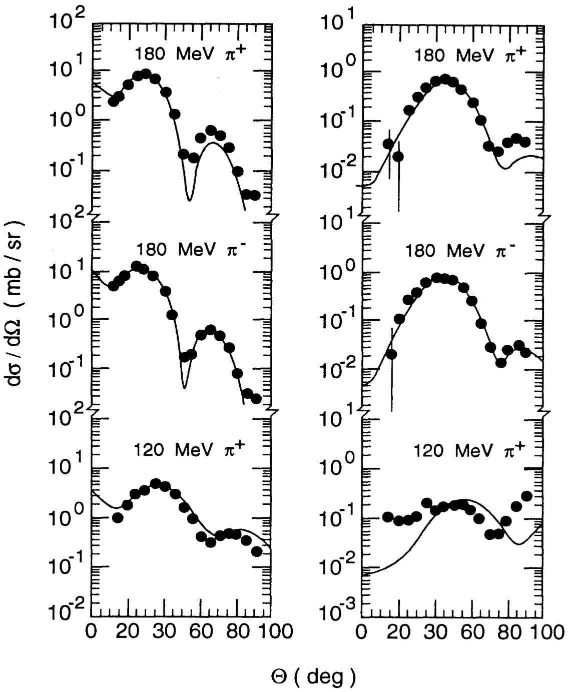

FIG. 3. Angular distributions for the 1.63-MeV 2^+ (left column) and the 4.25-MeV 4^+ (right column) states. The top graph in each column is 180-MeV π^+, the middle 180-MeV π^-, and the bottom 120-MeV π^+. The curves are DWIA calculations ([6]) using a collective-model transition density taken from [7].

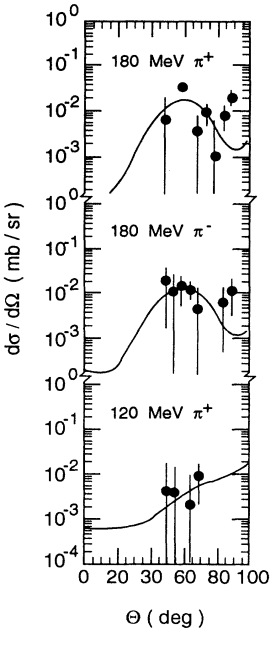

FIG. 4. Angular distributions for the 8.78-MeV 6^+ state. The top graph is 180-MeV π^+, the middle 180-MeV π^-, and the bottom 120-MeV π^+. The curves are DWPI calculations.

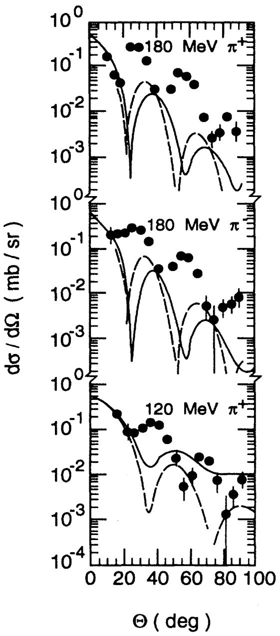

FIG. 5. Angular distributions for the 6.73-MeV 0^+ state. The top graph is 180-MeV π^+, the middle 180-MeV π^-, and the bottom 120-MeV π^+. The solid curve uses the standard collective-model transition density. The dashed curve uses the transition density of [17].

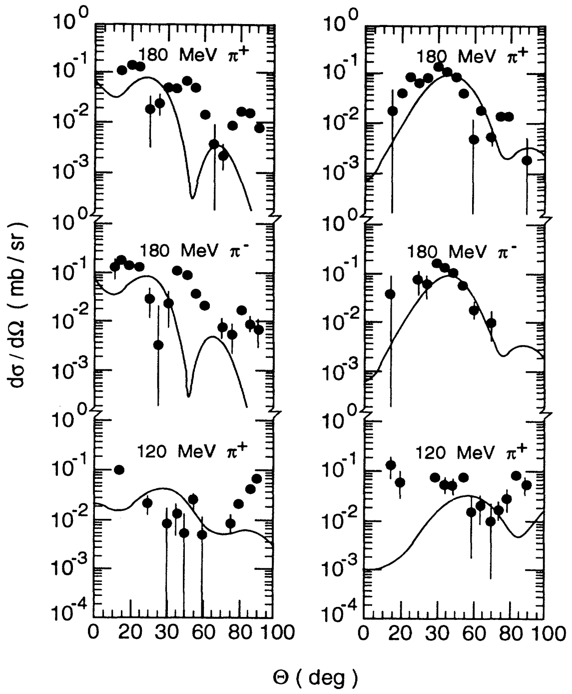

FIG. 6. Angular distributions for the 7.42-MeV 2^+ (left column) and the 9.99-MeV 4^+ (right column) states. The top graph in each column is 180-MeV π^+, the middle 180-MeV π^-, and the bottom 120-MeV π^+. The curves are DWPI calculations.

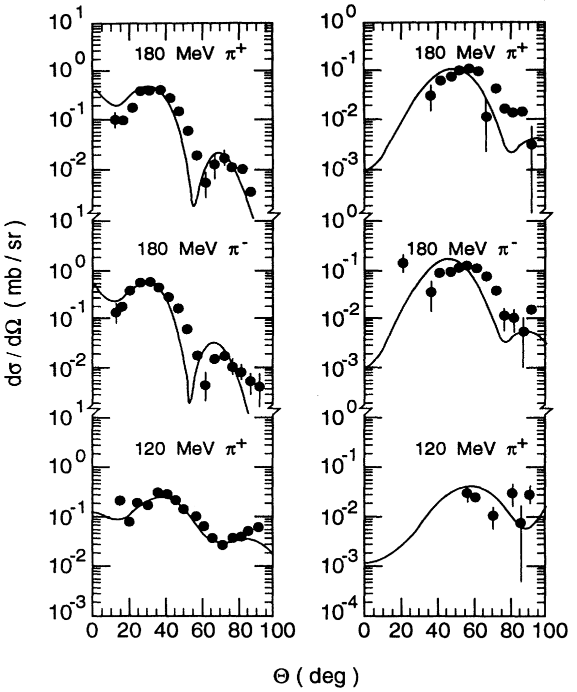

FIG. 7. Angular distributions for the 7.83-MeV 2^+ (left column) and the 9.03-MeV 4^+ (right column) states. The top graph in each column is 180-MeV π^+, the middle 180-MeV π^-, and the bottom 120-MeV π^+. The curves are DWPI calculations.

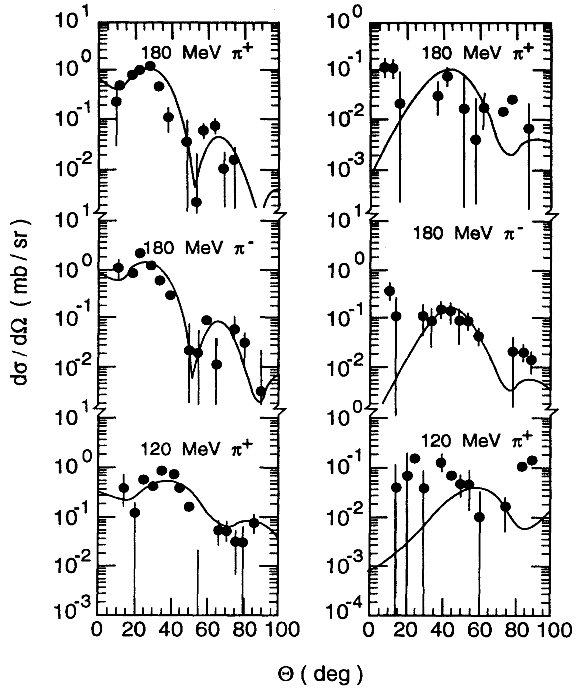

FIG. 8. Angular distributions for the 9.00-MeV 2^+ (left column) and the 10.79-MeV 4^+ (right column) states. The top graph in each column is 180-MeV π^+, the middle 180-MeV π^-, and the bottom 120-MeV π^+. The curves are DWPI calculations.

Grory (ZBM) to describe the structure of ^{16}O [11]. The *F* interaction of McGrory and Wildenthal [12] was used in the ZBM calculation. The third 0^+ band is believed to be either a $6p$-$2h$ or an $8p$-$4h$ excitation [10] so this band and the first two bands should be described by this calculation. The fourth 0^+ band is believed to be formed by exciting either two or four particles into the fp shell [19], and therefore should not be described by either of these calculations. Transition strengths from these calculations are included in Table I. Angular distributions calculated with these transition densities are compared with data in Figs. 9–15.

A. Ground-state band

The ground-state band contains three of the five strongest peaks in the spectra: the elastic, the 1.63-MeV 2^+, and the 4.25-MeV 4^+. The 8.78-MeV 6^+ is also present. The angular distributions for the 2^+, 4^+, and 6^+ are given in Figs. 3 and 4. The curves are distorted-wave impulse-approximation (DWIA) calculations with a collective transition density using the computer code DWPI [13]. The neutron and proton transition densities were assumed to be equal, both in shape and magnitude, and were taken to be a derivative of the ground-state charge

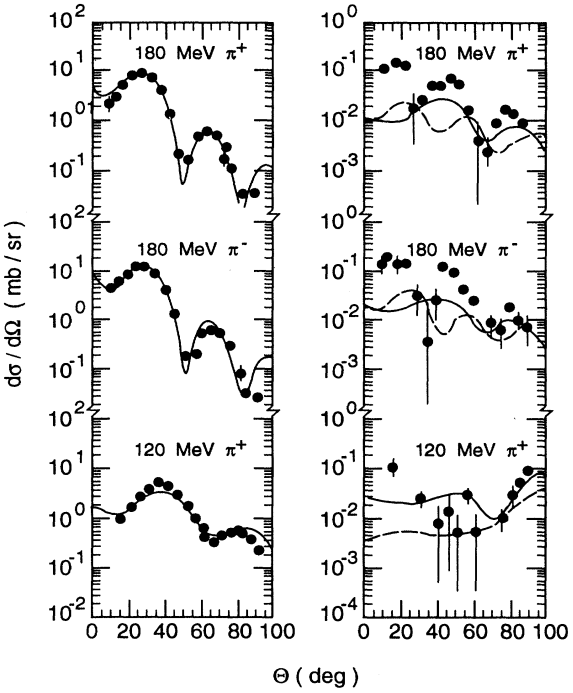

FIG. 9. Angular distributions for the 1.63-MeV and the 7.42-MeV 2^+ states. The top graph in each column is 180-MeV π^+, the middle 180-MeV π^-, and the bottom 120-MeV π^+. The curves are DWIA calculations using microscopic transition densities from the $(sd)^4$ shell-model calculation (solid) and ZBM (dashed).

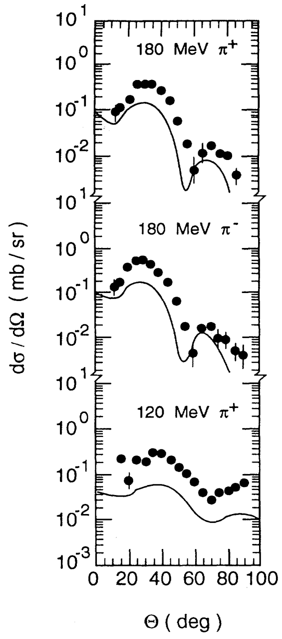

FIG. 10. Angular distributions for the 7.83-MeV 2^+ state compared with ZBM calculations.

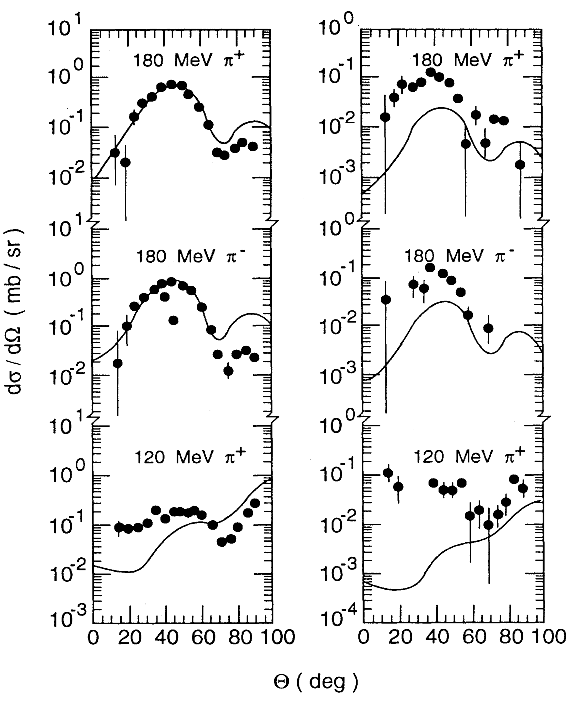

FIG. 11. Angular distributions for the 4.25-MeV and the 9.99-MeV 4^+ states. The top graph in each column is 180-MeV π^+, the middle 180-MeV π^-, and the bottom 120-MeV π^+. The curves are DWIA calculations using microscopic transition densities from the $(sd)^4$ shell-model calculation (solid) and ZBM (dashed).

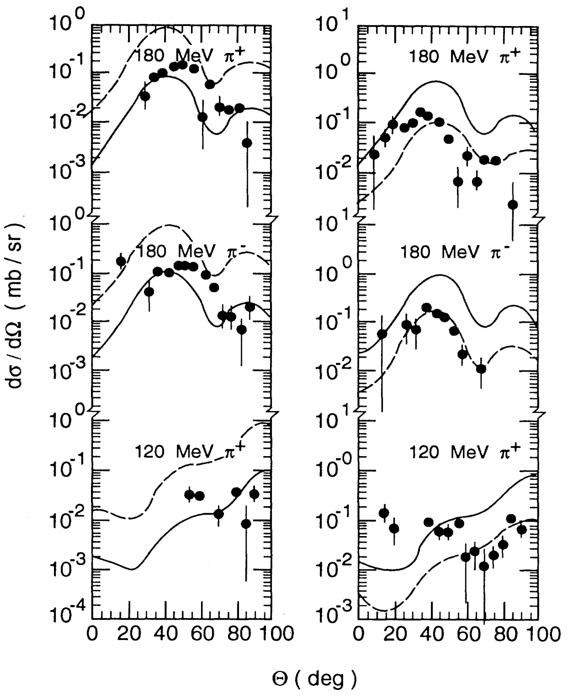

FIG. 12. Angular distributions for the 9.03-MeV and 9.99-MeV 4^+ states. The top graph in each column is 180-MeV π^+, the middle 180-MeV π^-, and the bottom 120-MeV π^+. The solid curves are DWIA calculations using microscopic transition densities from the ZBM shell-model calculation. Dashed curves assume the 4^+'s in the ZBM shell-model calculation switch as they do experimentally.

density which has been measured with electron elastic scattering [14]. The magnitude of the transition density was varied for each state to fit the three angular distributions. The transition strengths extracted from these fits are given in the last column of Table I. DWIA calculations using microscopic transition densities from the

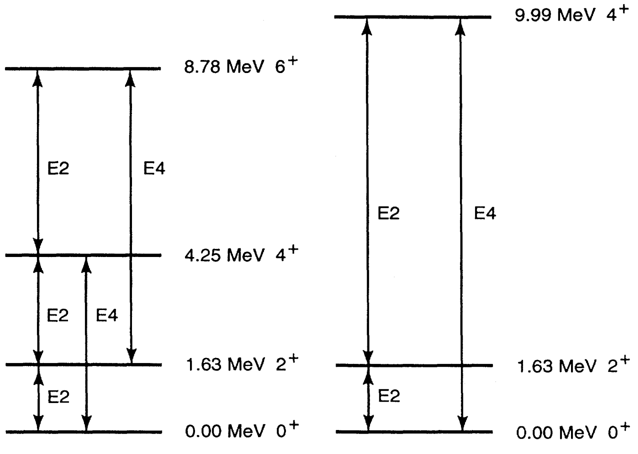

FIG. 13. Couplings used in the CCIA calculations.

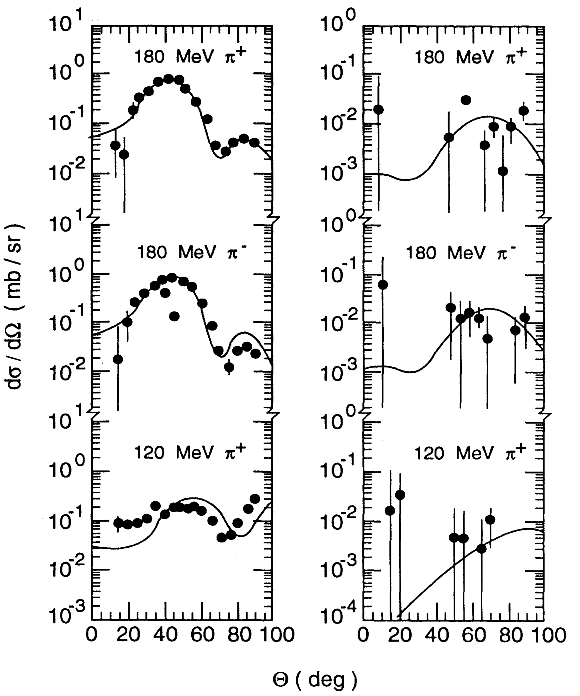

FIG. 14. CCIA calculations to the 4.25-MeV 4^+ (left column) and the 8.78-MeV 6^+ (right column) states. The top graph in each column is 180-MeV π^+, the middle 180-MeV π^-, and the bottom 120-MeV π^+.

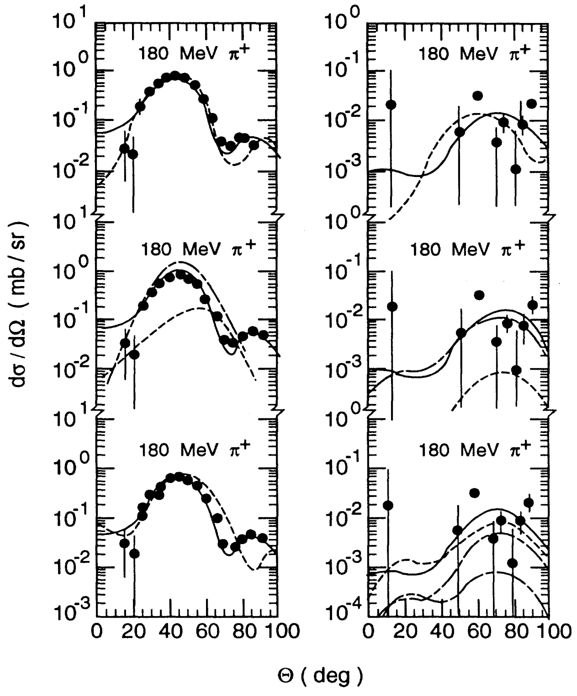

FIG. 15. CCIA calculations to the 4.25-MeV 4^+ (left column) and the 8.78-MeV 6^+ (right column) states. All of the graphs are 180-MeV π^+. The solid curve is the complete CCIA calculation in all six graphs. The dashed curves in the top graphs are DWPI calculations. In the middle graphs the dashed curves show the contributions of the different routes. In the bottom graphs the dashed curves show the effect of changing the relative phase.

shell-model calculations described above were performed using the codes PIPIT [15] and HL [16]. Data for the 1.63-MeV 2^+ and 4.25-MeV 4^+ states were used to extract the isoscalar $E2$ and $E4$ effective charges for both the $(sd)^4$ and ZBM calculations. They are given in Table II. With these effective charges, curves for the 1.63-MeV 2^+ state (Fig. 9) are indistinguishable for calculations with $(sd)^4$ and ZBM densities. The same is true for the 4.25-MeV 4^+ state (Fig. 11). An $E6$ transition is not possible in either model space.

It is somewhat surprising to observe the 6^+, since in the *sd* shell the largest single-particle transition allowed is $d \to d$ which gives $l = 4$, i.e., going to a 4^+ state. For this reason and because the $E2$ transitions between these states are known to be strong [1], coupled-channels impulse-approximation (CCIA) calculations have been done using the code NEWCHOP [17]. The couplings used are shown in Fig. 13 and their strengths are given in Table III. The results of these calculations are shown in Fig. 14. The calculations are absolutely normalized, but the strength of the $2^+ \to 6^+$ transition is not known and was assumed to be equal to the $0^+ \to 4^+$ strength. No $E6$ was used in the calculation, demonstrating that the state can be entirely populated by coupled-channels reaction routes.

Some of the details of the coupled-channels calculations are depicted in Fig. 15. The top graph in each column displays the CCIA calculation (solid curve) and the DWIA calculation (dashed curve). The main effect of the two-step route on the 4^+ calculation appears to be a shift in the position of the minimum. Destructive interference between the direct ($0^+ \to 4^+$) and the two-step ($0^+ \to 2^+ \to 4^+$, labeled 2P1 after the intermediate state) calculations is necessary to fit the 4^+ data, both in shape and normalization. In the second graph in each column the relative contribution of each route is given. The solid curve is the sum of all routes used, i.e., the entire calculation. For the 4^+, left column, the dashed curve is the 2P1 route and the dot-dashed curve is the direct route. The strength of the direct route was varied until the entire calculation reproduced the magnitude of the data. Because of the importance of the two-step route the effective charge extracted with the microscopic calculations may be up to 40% low. The strengths of the $E2$ transitions were fixed at the known values in the compilation [1]. The 6^+ calculation is dominated by the 4P1 route ($0^+ \to 4^+ \to 6^+$), shown by the alternating long- and short-dashed line in the middle graph. The dashed line is the

TABLE II. Isoscalar effective charges extracted for ZBM and $(sd)^4$ model spaces.

	Shell-model space	
l	$(sd)^4$	ZBM
2	2.0	2.2
4	2.2	~6[a]

[a] If the two-step contributions (destructive interference) to the 4.25-MeV cross section are taken into account these values could be up to 40% larger.

2P1 route ($0^+ \to 2^+ \to 6^+$). The strength of the $2^+ \to 6^+$ transition was assumed to be the same as the strength of the $0^+ \to 4^+$ transition. The $0^+ \to 2^+ \to 4^+ \to 6^+$ route is very weak. For the 4^+ calculation the choice of phase, $+1$ or -1, between the routes was straightforward as is obvious in the bottom graph. The dashed line gives the calculation with the opposite phase and the strength of the $E4$ transition varied to reproduce the overall magnitude of the data. Both the maximum and the minimum are at too large an angle. For the 6^+ calculation the phases chosen were those that gave the largest overall magnitude. With the addition of a direct $0^+ \to 6^+$ route any choice of phase can be made to fit the data if sufficient $E6$ strength is included.

B. 0_2^+ band

Three peaks seen in this experiment correspond to states in the $K^\pi = 0_2^+$ band. They are the 6.73-MeV 0^+, the only 0^+ excited state seen, the 7.42-MeV 2^+, which was observed in electron scattering to have an anomalous form factor [2], and the 9.99-MeV 4^+. Angular distributions and DWIA calculations for the 2^+ and 4^+ states are compared in Fig. 6. The 7.42-MeV peak has an anomalous angular distribution, as in electron scattering.

The $l = 4$ calculation does a reasonable job of reproducing the 9.99-MeV data, but the first maximum and minimum appear to be at a smaller angle than the DWIA calculation predicts. An $l = 3$ gives almost as good a fit to the data. The 9.99-MeV 4^+ has a strong $E2$ branch to the 1.63-MeV 2^+, so two-step calculations using the 1.63-MeV state as the intermediate state have been done. The couplings used are shown in Fig. 13 and their strengths given in Table III. The strength of the $l = 4$ transition was chosen to fit the data. These calculations significantly improve the fit to the 9.99-MeV state as shown in the left column of Fig. 16. The CCIA calculation does a very good job of fitting the 9.99-MeV data. The top graph of the right column of Fig. 16 contains a comparison of the CCIA (solid line) and DWIA (dashed line). The middle graph gives the contributions of the direct (dot-dashed line) and 2P1 (dashed line) routes and their sum (solid line). Again destructive interference was necessary to fit the angular distribution. The bottom graph presents the results with constructive interference (dashed line). Constructive interference pushes the maximum and minimum to larger angles.

The radial form of the collective transition density used for $E2$, $E4$, and $E6$ transitions is incorrect for $l = 0$ transitions, because the integral of the $E0$ transition density must be zero from orthogonality [18]. Figure 17 compares the standard collective transition density (solid line) and the transition density of Auerbach [18] (dashed line). While these transition densities look very different they produce very similar results for the angular distributions, as noted in Fig. 5. This is probably because the pion sees only the surface of the nucleus and on the surface these transition densities are very similar. In elec-

TABLE III. Transition strengths used in CCIA calculations.

E_i (MeV)	E_f (MeV)	Δl	$B(E_i \to E_f, \Delta l)$ ($e^2\,\mathrm{fm}^{2\lambda}$)
0.0	1.63	2	323^a
1.63	4.25	2	129^a
0.0	4.25	4	7730
1.63	6.73	2	2.4^a
0.0	6.73	0	$M=5.27^b$
1.63	7.42	2	5.5^a
4.25	8.78	2	2.4^a
1.63	8.78	4	1550^c
1.63	9.03	2	34^a
0.0	9.03	4	1830
1.63	9.99	2	49^a
0.0	9.99	4	1640

[a] These matrix elements were fixed by other data. For transitions from the ground state, results from the DWIA calculations in Table I were used. All other transition strengths were taken from [1].

[b] M is defined in the text for $l = 0$ transitions.

[c] This matrix element was constrained to equal the 0.0→4.25 matrix element.

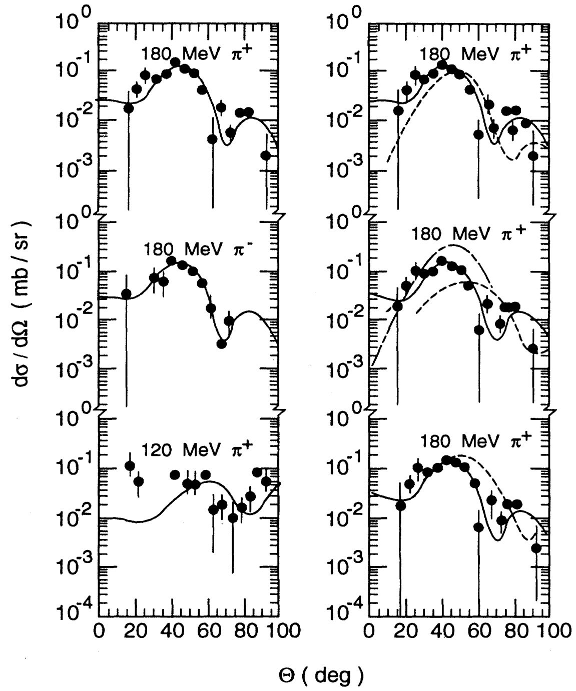

FIG. 16. CCIA calculations to the 9.99-MeV 4^+ state. The solid curve is the complete CCIA calculation in all six graphs. The top graph in left column is 180-MeV π^+, the middle 180-MeV π^-, and the bottom 120-MeV π^+. In the right column all of the graphs are 180-MeV π^+. The dashed curve in the right top graph is a DWPI calculation. In the right middle graph the dashed curves show the contributions of the different routes. In the right bottom graph the dashed curve shows the effect of changing the relative phase.

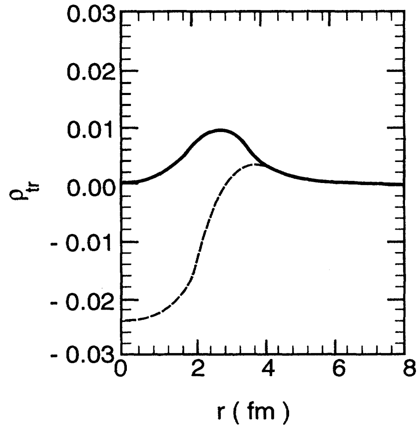

FIG. 17. $l = 0$ transition densities used for the 6.73-MeV 0^+ state.

tron scattering a phenomenological transition density of the form

$$\rho_{\rm tr} = \rho_0(1 + ar^2 + br^4 + cr^6)\exp\left(-\frac{r^2}{\beta^2}\right)$$

was used [2]. With the constraint that c=0, then knowing M and $R_{\rm tr}$, where

$$M = \langle r^2 \rangle ,$$

$$M = \sqrt{4\pi}\int r^2 \rho_{\rm tr} r^2 dr ,$$

and

$$R_{\rm tr}^2 = \frac{\langle r^4 \rangle}{\langle r^2 \rangle}$$

fixes ρ_0, a, and b. Using M=7.37±1.97 fm^2 and $R_{\rm tr}$=5.73±1.30 fm or M=5.85±1.5 fm^2 from electron scattering, a DWIA calculation can reproduce the magnitude of the data. The $0^+ \rightarrow 2^+ \rightarrow 0^+$ (2P1) two-step route is important near the minima of the data. Varying these parameters, allowing terms up to r^6, and including the two-step route gives the curves shown in Fig. 18. The best fit, shown in the left column of Fig. 18, finds M=5.27±0.04 fm^2 and $R_{\rm tr}$=5.95±0.07 fm. The errors are statistical errors only. The polynomial in r, together with variations in $R_{\rm tr}$, produce curves somewhat different from those in Fig. 5. The top graph in the right column of Fig. 18 has the contribution of the direct and the bottom the two-step for the 180-MeV π^+ calculation. If c is set equal to zero, the fit is not as good, although still very good, and the extracted M and $R_{\rm tr}^2$ are changed by an amount much less than the statistical error of the original fit.

The 7.42-MeV 2^+ has a strong decay to the 1.63-MeV 2^+. Using the 1.63-MeV 2^+ as the intermediate state, the two-step route, the solid curve in Fig. 19, is clearly non-negligible, especially around the minima. Unfortunately, it is not possible to fit the data including a direct route using the standard collective-model transition density. The dashed curves in Fig. 19 show the two-step and direct routes added and subtracted coherently, limiting the strength of the direct route to the upper limit

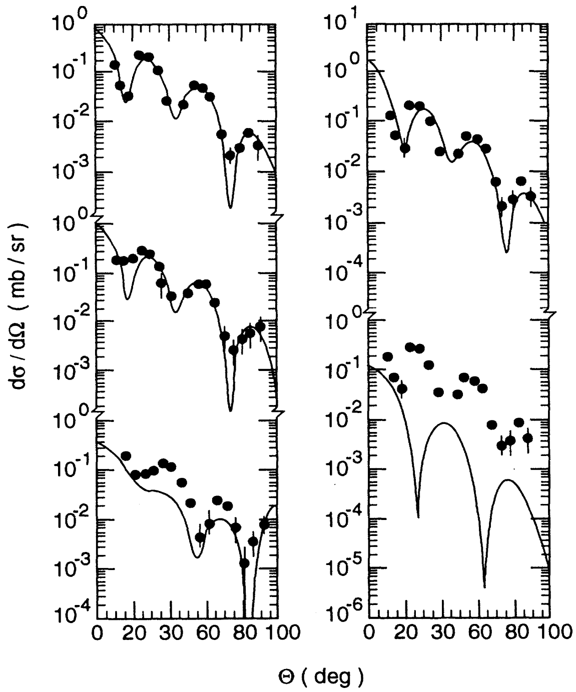

FIG. 18. CCIA calculations to the 6.73-MeV 0^+ state. The top graph in left column is 180-MeV π^+, the middle 180-MeV π^-, and the bottom 120-MeV π^+. In the right column all of the graphs are 180-MeV π^+. The curve in the right top graph is the direct component of the CCIA calculation. In the right bottom graph the curve is the 2P1 component of the CCIA calculation.

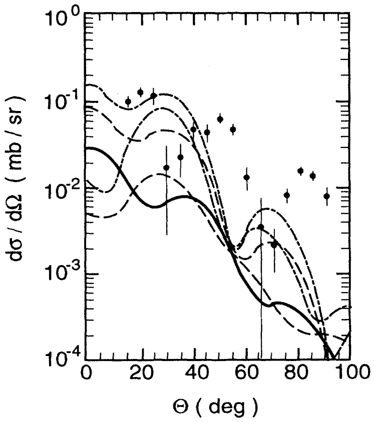

FIG. 19. CCIA calculations to the 7.42-MeV 2^+ state for 180-MeV π^+ incident beam. The solid curve is the 2P1 route. The dashed curves are the 2P1±DIR routes, with the direct strength at the upper limit in the compilation ([1]). The dot-dashed curves are the 2P1±DIR routes, with the direct strength increased to fit the magnitude of the data.

in the compilation [1]. If the strength of the direct route is increased, the CCIA calculation can be made to reproduce the magnitude of the data, the dot-dashed curves in Fig. 20, but not the shape of the angular distribution. The 7.42-MeV state also has a weak decay to the 4.25-MeV 4^+ state, but that route is at least an order of magnitude smaller than the lowest 180-MeV π^+ data point. No decay from the 7.42-MeV state to the 6.73-MeV 0^+ state has been seen [1], but since both states are in the same rotational band a two-step calculation using the 6.73-MeV 0^+ state as the intermediate state was also done. The transition between the 7.42-MeV state and the 6.73-MeV state has to be at least three times the strength of the transition between the 1.63-MeV state and the ground state to have any significant effect.

Using a microscopic transition density in a DWIA calculation does a better job of reproducing the angular distribution of the 7.42-MeV state, as shown in Fig. 9. The effective charges found for the 1.63-MeV 2^+ state were used to normalize the calculations. Both the ZBM and $(sd)^4$ calculations give transition densities which have some of the anomalous characteristics of the data. The peculiar angular distribution of the 7.42-MeV 2^+ state appears to arise from destructive interference between the $1d_{5/2} \to 1d_{5/2}, 1d_{5/2} \to 2s_{1/2}$, and $2s_{1/2} \to 1d_{5/2}$ amplitudes in the shell-model calculations. Shown in Fig. 12 are microscopic calculations to the 9.99-MeV 4^+ state. The $(sd)^4$ calculation underpredicts the 9.99-MeV 4^+ state by about an order of magnitude, but two-step contributions were important for this state. The CCIA calculations required a larger direct contribution, making the underprediction worse. In the ZBM calculation there is some difficulty deciding whether the second or third model state corresponds to the 9.99-MeV state. A discussion of this calculation will be included in the discussion on the 9.03-MeV 4^+ state.

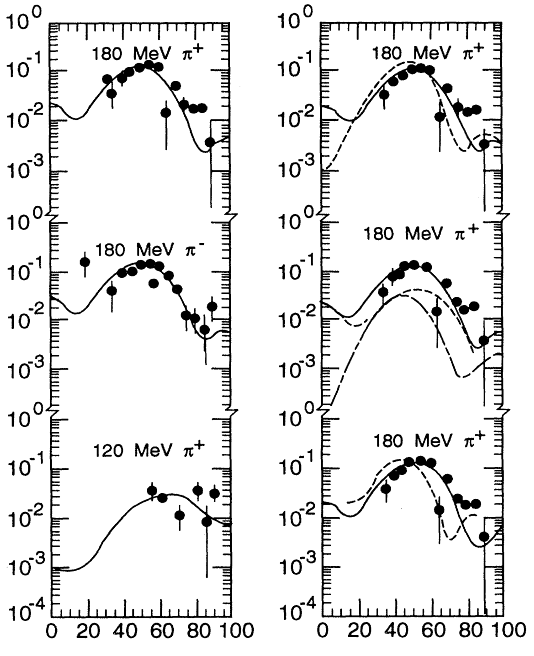

FIG. 20. CCIA calculations to the 9.03-MeV 4^+ state. The top graph in the left column is 180-MeV π^+, the middle 180-MeV π^-, and the bottom 120-MeV π^+. In the right column all of the graphs are 180-MeV π^+. The dashed curve in the right top graph is a DWPI calculation. In the right middle graph the dashed curves show the contributions of the different routes. In the right bottom graph the dashed curve shows the effect of changing the relative phase.

C. 0_3^+ band

The 7.83-MeV 2^+ and 9.03-MeV 4^+ members of the $K^\pi = 0_3^+$ band are shown in Fig. 7. DWIA calculations reproduce both angular distributions reasonably well, and the extracted matrix elements are given in Table I. The first maximum and minimum for both states are at larger angles than in the calculation. Both states have a strong $E2$ decay to the 1.63-MeV 2^+ state, so two-step calculations were done. The $0^+ \to 2^+ \to 2^+$ calculation is negligibly small and unable to improve the fit. On the other hand, $0^+ \to 2^+ \to 4^+$ is important, as demonstrated in Fig. 20. The contribution of this route (the dashed line in the middle graph of the second column) is comparable to the contribution of the direct route, the dot-dashed line. The left column gives the results of the coupled-channels calculation using both the 2P1 and direct routes, varying the strength of the direct route to fit the data.

The strengths used are given in Table III. Constructive interference was necessary to push the maximum and minimum to a larger angle and fit the data. The states in this band are believed to involve excitation of particles out of the ^{16}O core, so they are not included in the $(sd)^4$ calculation. Using the $E2$ effective charge from the 1.63-MeV 2^+ state for the 7.83-MeV 2^+ state the calculation slightly underpredicts the data, shown in Fig. 10. There was some confusion in the ZBM calculation as to whether the second model state corresponded to the second or third physical state, and similarly for the third model state. Figure 12 shows the results of each choice. Ignoring two-step contributions the third model state is able to fit either the second or the third 4^+ angular distribution, but the second model state overpredicts both by a factor of 5–10. However, the CCIA calculations possessed constructive interference for the 9.03-MeV 4^+ state and destructive interference for the 9.99-MeV 4^+ state, so assuming the second model state goes with the third 4^+ and the third model state goes with the second 4^+, i.e., assuming the bands cross in the ZBM space as they do in the physical space, gives better agreement with the data, although both calculations are probably still too large.

D. 0_4^+ band

It is somewhat surprising that the 2^+ and 4^+ states in the fourth $K^\pi = 0^+$ band were excited in pion inelastic scattering. This band is believed to result from the excitation of two or four particles into the fp shell. Since the pion interaction with the nucleus is a one-body operator, this state should not be excited unless its wave function has some $(sd)^4$ components or that of the ground state has some $(fp)^2$ or $(fp)^4$ components. Both of these states have large α widths and no γ decays are known for either of them. The compilation [1] lists $E_x \sim 8.8$ MeV and $\Gamma > 800$ keV for the 2^+ and $E_x = 10.80 \pm 0.075$ MeV and $\Gamma = 350$ keV for the 4^+. Values of $E_x = 9.00 \pm 0.18$ MeV and $\Gamma = 800$ keV for the 2^+ and $E_x = 10.79$ MeV and $\Gamma = 350$ keV for the 4^+ fit the current data. Because of their large widths these states have not been extensively studied. Both the 2^+ and 4^+ states, along with the 0^+ state at 8.3 MeV which is not seen here, are seen in ^{16}O(α,α) and ^{19}F(^{3}He,d), and the 4^+ state has also been seen in ^{16}O(^{6}Li,d) [1]. Mixing between the 8.3-MeV 0^+ and the 6.73-MeV 0^+ states and between the 9.0-MeV 2^+ and the 7.42-MeV 2^+ states can explain the (^{3}He,d) data [19,20], but that mixing is unable to explain the present data. The structure of the 9.00-MeV state is discussed in more detail in [7]. Angular distributions for these states are compared with DWIA calculations in Fig. 8. The matrix elements extracted from these fits are listed in Table I. The maximum and minimum are at a larger angle in the DWIA calculation than in the data for the 2^+. It has been demonstrated in previous sections that CCIA calculations can shift the maximum and minimum, but since no couplings between this state and other states are known it is not possible to do a useful calculation.

IV. CONCLUSIONS

This work is a study of pion inelastic scattering on ^{20}Ne to states in the first four $K^\pi = 0^+$ bands. Many of the extracted angular distributions can be explained using the distorted-wave impulse approximation (DWIA) and a collective transition density. For some peaks DWIA was inadequate, or gave results that contradicted information previously known about those states. Coupled-channels impulse-approximation (CCIA) calculations were done to explain the transitions to many of those states.

For strong transitions, DWIA using a collective transition density fits the data very well and gives results that agree with other probes. While DWIA does sometimes work for weaker transitions, this is not always the case. Two-step routes, even when they are much weaker than the direct route, can have a dramatic effect on the extracted transition matrix element, $M_{p,n}$. Stronger two-step routes can change the shape of the angular distribution, moving maxima and minima enough that one might deduce an incorrect l transfer. When one or more two-step routes dominate, very anomalous and misleading angular distributions can result. Also important for weaker peaks are microscopic effects. Cancellations between shell-model amplitudes can give very anomalous angular distributions which in regions where the density of states is high might lead one to incorrectly deduce the peak is a doublet.

This work was supported in part by the National Science Foundation, the United States Department of Energy, and the Robert A. Welch Foundation.

[1] F. Ajzenberg-Selove, Nucl. Phys. **A475**, 1 (1987).
[2] S. Mitsunobu and Y. Torizuka, Phys. Rev. Lett. **28**, 920 (1972).
[3] R. P. Singhal, H. S. Caplan, J. R. Moreira, and T. E. Walker, Can. J. Phys. **51**, 2125 (1973).
[4] G. S. Blanpied, B. G. Ritchie, M. L. Barlett, R. W. Fergerson, G. W. Hoffmann, J. A. McGill, and B. H. Wildenthal, Phys. Rev. C **38**, 2180 (1988); G. S. Blanpied, G. A. Balchin, G. E. Langston, B. G. Ritchie, M. L. Barlett, G. W. Hoffmann, J. A. McGill, M. A. Franey, M. Gazzaly, and B. H. Wildenthal, *ibid.* **30**, 1233 (1984); R. de Swiniarski, A. Genoux-Lubain, G. Bagieu, J. F. Cavaignac, and D. H. Worledge, Phys. Lett. **43B**, 27 (1973).
[5] H. Rebel, G. W. Schweimer, J. Specht, G. Schatz, R. Löhken, D. Habs, G. Hauser, and H. Klewe-Nebenius, Phys. Rev. Lett. **26**, 1190 (1971); A. Springer and B. G. Harvey, *ibid.* 14, 316 (1965).
[6] G. Rowe, M. Salomon, and R. H. Landau, Phys. Rev. C **18**, 584 (1978).
[7] M. Burlein *et al.*, Phys. Rev. C **40**, 785 (1989).
[8] B. A. Brown, A. Etchegoyen, and W. D. M. Rae, OXBASH computer code (1985).
[9] B. H. Wildenthal, Prog. Part. Nucl. Phys. **11**, 5 (1984).
[10] H. T. Fortune, in *Nuclear Spectroscopy with Heavy Ion Reactions*, Proceedings of the Heavy Ion Summer Study Oak Ridge National Laboratory, edited by, S. T. Thornton (Plenum, New York, 1972), pp. 353–377; H. T. Fortune (unpublished).
[11] A. P. Zuker, B. Buck, and J. B. McGrory, Phys. Rev. Lett. **21**, 39 (1968).
[12] J. B. Grory and B. H. Wildenthal, Phys. Rev. C **7**, 974 (1973).
[13] R. A. Eisenstein and G. A. Miller, Comput. Phys. Commun. **11**, 95 (1976).
[14] H. DeVries, C. W. DeJager, and C. DeVries, At. Nucl. Data Tables **36**, 495 (1987).
[15] R. A. Eisenstein and F. Tabakin, Comput. Phys. Commun. **12**, 237 (1976).
[16] T.-S. H. Lee and R. D. Lawson, Phys. Rev. C **21**, 679 (1980); T.-S. H. Lee and D. Kurath, *ibid.* **21**, 293 (1980); T.-S. H. Lee and F. Tabakin, Nucl. Phys. **A226**, 253 (1974).
[17] C. L. Morris, private communication.
[18] N. Auerbach, Phys. Lett. **36B**, 293 (1971).
[19] H. T. Fortune, R. Middleton, and R. R. Betts, Phys. Rev. Lett. **29**, 728 (1972).
[20] H. T. Fortune, R. R. Betts, and R. Middleton, Phys. Lett. **62B**, 282 (1976).